Nanoscale

PAPER

View Article Online
View Journal | View Issue

Cite this: *Nanoscale*, 2025, **17**, 25859

Formamidinium-based Pb–Sn mixed-halide perovskite solar cells with near-optimal bandgap: $FAPb_{1-x}Sn_x(I_{0.8}Br_{0.2})_3$

Yan Chen,[a] Ying Fan Tay,[b] Mingjie Li,[c] Than Zaw Oo,[d] Sing Yang Chiam,[e] Yeng Ming Lam,[f] Tze Chien Sum[g] and Lydia Helena Wong *[f,h]

Received 1st July 2025,
Accepted 8th October 2025

DOI: 10.1039/d5nr02776d

rsc.li/nanoscale

The development of lead–tin (Pb–Sn) binary perovskites with ideal bandgaps (1.3–1.4 eV) is crucial for single-junction perovskite solar cells (PSCs) to approach the Shockley–Queisser efficiency limit. Compositional engineering, the most effective strategy for improving PSC efficiency, offers a promising route to tune the perovskite bandgap into the ideal range. In this study, we developed FA-based Pb–Sn mixed-halide perovskites, $FAPb_{1-x}Sn_x(I_{0.8}Br_{0.2})_3$, *via* compositional engineering to target near-optimal bandgaps (~1.4 eV), improve crystallinity and enhance absorption coefficient. Structural and morphological analyses reveal that Sn incorporation stabilizes the photoactive phase of pure FA-based perovskites, whereas Pb incorporation promotes the formation of dense films. This synergistic effect enables Pb–Sn binary PSCs to outperform their Pb-only and Sn-only counterparts. Furthermore, it is found that a Sn content of x = 0.4 yields optimal photovoltaic performance under ambient conditions and the lowest photovoltage deficit. Our analysis of the charge recombination processes indicates that structural disorder and band alignment act as competing factors governing the photovoltage deficit. This study elucidates how compositional engineering fine-tunes the optoelectronic properties of perovskites and provides insights into developing novel Pb–Sn binary PSCs with near-optimal bandgaps.

Introduction

In recent years, the photovoltaic field has been captivated by the rapid advancements in perovskite solar cells (PSCs), with significant breakthroughs not only in boosting power conversion efficiency (PCE) but also in mitigating environmental concerns associated with traditional materials.[1–3] To address the toxicity concerns, lead (Pb) has been substituted with tin (Sn) or germanium (Ge) at the metal site.[4–7] Nonetheless, superior efficiency and long-term stability are sacrificed in absolutely Pb-free PSCs. Alternatively, alloying Pb and Sn in perovskites can not only reduce the content of toxic Pb element but also narrow the bandgap.[8–11] Developing Pb–Sn binary perovskites with an ideal bandgap of 1.3–1.4 eV offers a promising route to approach the Shockley–Queisser (SQ) limit for low-toxic single-junction solar cells.[12] Notably, 1.4 eV-bandgap PSCs are ideal for use as the bottom cell in eco-friendly Pb-less, four-terminal tandem solar cells.[13,14] Hence, there is a pressing need to develop perovskite materials with ideal or near-optimal bandgaps. More importantly, balancing Sn content to minimize non-radiative losses while maintaining phase purity and interfacial alignment is critical for unlocking the full potential of optimal bandgap perovskites.

Formamidinium (FA)-based halide perovskites have emerged as superior candidates over methylammonium (MA) counterparts due to their enhanced thermal stability, excellent crystallinity, and optimal bandgap.[15–17] In addition, the incorporation of bromide (Br) has been recognized as an effective strategy for tuning the bandgap and enhancing the photovoltage, thereby optimizing the device performance.[14,18–20] For example, it has been reported that introducing Br into $MAPb_{0.4}Sn_{0.6}I_3$ perovskites suppresses trap-assisted recombina-

[a]*School of Materials Science and Engineering, Shandong University, Jinan, Shandong 250061, China*
[b]*Institute of Sustainability for Chemicals, Energy and Environment (ISCE2), Agency for Science, Technology and Research (A*STAR), 1 Pesek Road Jurong Island, Singapore, 627833, Singapore*
[c]*Department of Applied Physics, The Hong Kong Polytechnic University, Kowloon 999077Hong Kong, China*
[d]*Universities' Research Centre, University of Yangon, Yangon 11041, Myanmar*
[e]*Institute of Materials Research and Engineering, Agency for Science, Technology and Research, 2 Fusionopolis Way, Singapore 138634, Singapore*
[f]*School of Materials Science and Engineering, Nanyang Technological University, 50 Nanyang Avenue, Singapore 639798, Singapore. E-mail: LydiaWong@ntu.edu.sg*
[g]*Division of Physics and Applied Physics, School of Physical and Mathematical Sciences, Nanyang Technological University, 21 Nanyang Link, Singapore 637371, Singapore*
[h]*Energy Research Institute @NTU (ERI@N), Research Techno Plaza, X-Frontier Block, 50 Nanyang Drive, Singapore 637553, Singapore*

tion, leading to a significant enhancement in photovoltage and a record efficiency of 12.1% for Sn-rich (≥60%) PSCs at that time.[20] Furthermore, $CsPb_{0.4}Sn_{0.6}I_{2.4}Br_{0.6}$ PSCs demonstrate lower non-radiative recombination states than their triiodide analogues, leading to a champion PCE of up to 12.34%.[21] Thus far, the partial substitution of Pb with Sn has been widely applied in MA/Cs-based mixed-halide perovskite systems for Pb reduction and bandgap tuning.[20–23] However, few efforts have been devoted to developing FA-dominant Pb–Sn binary perovskite compositions with I–Br blending.

In this work, we have systematically investigated the compositional effect of Sn content on the structural, morphological, and optical properties of perovskite films in a purely FA-based mixed-halide perovskite system, $FAPb_{1-x}Sn_x(I_{0.8}Br_{0.2})_3$ (x = 0, 0.2, 0.4, 0.6, 0.8, and 1.0). The fabrication approach for these perovskite films is schematically illustrated in Fig. 1a. Compared with their pure Pb/Sn-based counterparts, Pb–Sn binary perovskite films exhibited a photoactive perovskite phase and dense coverage. Among our newly developed Pb–Sn binary perovskite films, those with x = 0.4 and 0.6 demonstrated near-optimal bandgaps approaching 1.4 eV, along with higher crystallinity and absorption coefficients. Accordingly, the PSCs with x = 0.4 and 0.6 delivered higher PCEs than the devices with alternative compositions. Despite their near-optimal bandgaps, these PSCs suffered from notable photovoltage deficits, limiting overall device performance. To gain deeper insight into these limitations, we investigated there combination mechanisms in both the perovskite film and the complete device stack using comprehensive spectroscopic characterization. Our findings reveal that structural disorder and band alignment acting as two competing factors influence the photovoltage deficit.

Experimental section

Materials

PbI_2 (99.999%) was purchased from Tokyo Chemical Industry; SnI_2 (99.99%) and all the organic solvents, including dimethylformamide (DMF) and dimethyl sulfoxide (DMSO) *etc.*, were purchased from Sigma Aldrich; $HC(NH_2)_2I$ (FAI) and $HC(NH_2)_2Br$ (FABr) were purchased from Dyesol; poly(3,4-ethylenedioxythiophene) polystyrenesulfonate (PEDOT:PSS) solution was purchased from Heraeus Limited; phenyl-C_{61}-butyric acid methyl ester ($PC_{61}BM$) and bathocuproine (BCP) were purchased from Nano-C. All the aforementioned chemicals were used as received.

Film and device fabrication

All the substrates, including pre-patterned ITO glass, quartz and glass slice, were cleaned with Decon soap, deionized water, ethanol and isopropanol sequentially by ultra-

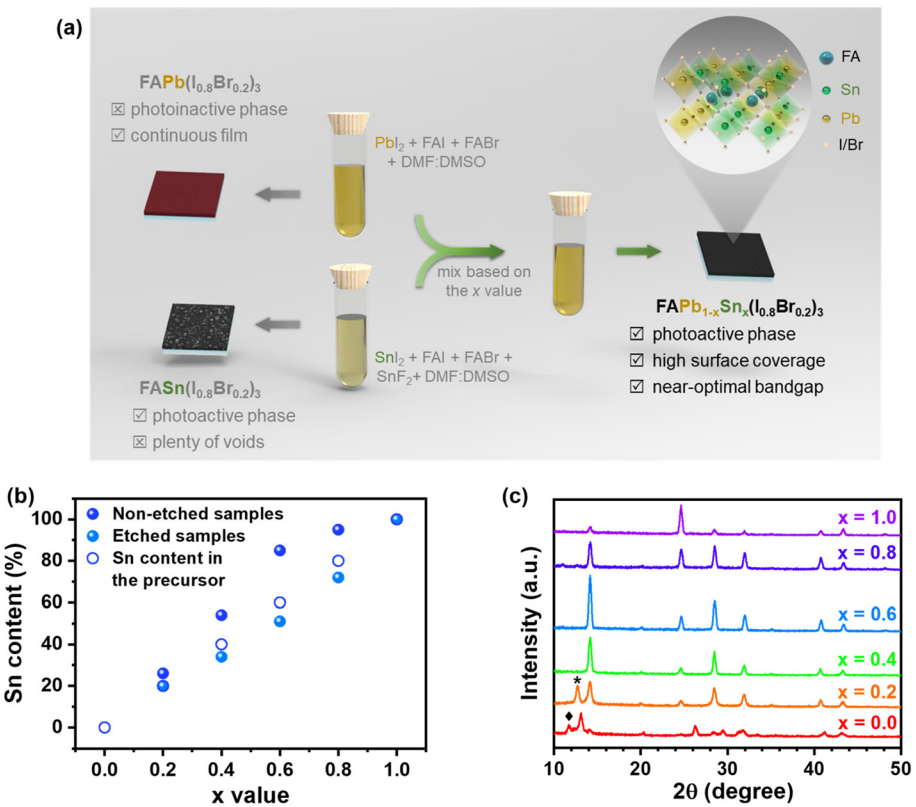

Fig. 1 Film characterization. (a) Schematic illustration of the fabrication approach for Pb–Sn binary perovskite films. (b) Comparison of Sn contents for samples before and after etching, obtained by XPS characterization. (c) XRD patterns of $FAPb_{1-x}Sn_x(I_{0.8}Br_{0.2})_3$ (x = 0, 0.2, 0.4, 0.6, 0.8, and 1.0) perovskite films.

sonication. The cleaned substrates were treated with ozone for 15 min prior to use. The as-received PEDOT:PSS solution (aqueous dispersion, 1 : 6 w/w) was filtered through a PES membrane (0.45 μm). After filtering, the undiluted solution was spin-coated onto the glass/ITO substrates at 3000 rpm for 60 s. The substrates were then transferred into a nitrogen (N_2) glovebox and annealed at 150 °C for 10 min.

In this study, the 20% bromide was introduced into the I/Br mixed-halide system through FABr. For the precursor solution of $FAPb(I_{0.8}Br_{0.2})_3$, 1.2 mmol PbI_2, 0.48 mmol FAI and 0.72 mmol FABr were dissolved in a 1 mL mixed solvent of DMF : DMSO (v : v = 4 : 1). Similarly, the $FASn(I_{0.8}Br_{0.2})_3$ precursor solution was prepared by dissolving 1.2 mmol SnI_2, 0.48 mmol FAI, and 0.72 mmol FABr in 1 mL of a mixed solvent of DMF : DMSO (v/v = 4 : 1). As a common strategy applied in the fabrication of Sn-containing PSCs, 10 mol% SnF_2 was added to inhibit the Sn(II) oxidation.[24] Subsequently, the Pb-based and Sn-based precursor solutions of the same concentration were mixed based on the designed x values to obtain the target compositions (*i.e.* $FAPb_{1-x}Sn_x(I_{0.8}Br_{0.2})_3$, where x = 0.2, 0.4, 0.6, and 0.8). The perovskite film was deposited *via* a single-step spin-coating method with antisolvent dripping. In brief, the perovskite solution was spin-coated at 5000 rpm for 55 s and the antisolvent diethyl ether was fast dripped onto the spinning substrate 20 s before the end. Subsequently, all resulting substrates were annealed at 100 °C for 10 min, except for the neat Pb-based substrate (150 °C for 10 min). When preparing the sample for UV-Vis absorption measurements, the perovskite film was deposited on quartz. For the other film characterizations, the perovskite film was prepared on glass. To minimize the deterioration in air, the perovskite films were coated with a poly(methyl methacrylate) (PMMA) layer by drop-casting.

Prior to use, the $PC_{61}BM$ solution in chlorobenzene (20 mg mL^{-1}) was kept at 70 °C under stirring overnight. Then, the fully dissolved $PC_{61}BM$ solution was spin-coated at 2000 rpm for 90 s. Finally, an 8 nm BCP layer and a 70 nm silver layer were evaporated under high vacuum.

Characterization

Crystallographic data were collected using an X-ray diffractometer (PANalytical XPert Pro) with Cu Kα radiation and at a step of 0.02°. Topographical images were recorded by a field-emission scanning electron microscope (FESEM, JEOL, JSM 7600F) with an accelerating voltage of 5 kV. Absorption spectra were acquired by UV-Vis-NIR Lambda 950 equipped with an integrating sphere attachment. Assuming uniform attenuation, the absorption coefficients (α) were calculated using the expression of $\alpha = (A \cdot \ln 10)/t$, where A is the absorbance and t denotes the film thickness. X-ray photoelectron spectroscopy (XPS) was performed using a Theta Probe system (ESCALab 250i-XL & ThetaProbe A1333) at a base pressure below 5×10^{-10} mbar with a monochromatic Al Kα (1486.7 eV) X-ray source. Transient absorption spectroscopy (TAS) measurement was conducted using a Helios™ setup (Ultrafast Systems LLC) with chirp-correction. The probe beam (white-light continuum in the range of 400–800 nm) was generated from a sapphire crystal (3 mm) using a Coherent Libra™ laser system (150 fs FWHM, 80 MHz repetition rate, 800 nm fundamental wavelength). The 400 nm pump beam was generated by frequency-doubling the 800 nm fundamental beam using a BBO crystal. The spot diameter of pump-beam on the sample was ~2 mm. TAS signals were collected using a detector with a CMOS sensor.

The photocurrent–voltage (J–V) characteristics were recorded using a digital sourcemeter (Keithley 2400) and a solar simulator (SAN-EI XES-301S, AAA) under AM 1.5G standard conditions. A shadow mask with an aperture of 0.0625 cm^2 was applied during measurement. In light-intensity-dependent J–V measurements, neutral-density filters were employed to vary the light intensity. External quantum efficiency (EQE) spectra were measured using a lock-in amplifier (Stanford Research Systems, SRS 810). The light source was provided by a Newport 300 W Xenon lamp passing through a 17 Hz mechanical chopper wheel and a monochromator (Oriel Cornerstone 130). Note that all unencapsulated solar cells were measured in ambient air at 63 ± 3% relative humidity. Electrochemical impedance spectroscopy (EIS) was performed in a N_2-filled glovebox with an Autolab PGSTAT302N. The frequency was swept from 1 MHz to 10 Hz at zero bias under 0.9 sun illumination.

Results and discussion

Compositional engineering of Pb–Sn perovskite films

The Sn composition of perovskite film with x = 0.2–1.0 was measured by XPS. Typically, the elemental composition determined by XPS originates from the top ~10 nm of the examined film. To further study the Sn composition at a deep position (~10 nm depth into the bulk), argon etching was performed until the adventitious carbon signal disappeared. The obtained XPS peaks of Sn 3d core level are shown in Fig. S1, and the Sn contents at the film surface before and after etching are compared in Fig. 1b. Interestingly, all Pb–Sn binary perovskite films exhibited significantly higher Sn contents at the top surface (before etching) and lower Sn contents at ~10 nm depth into the bulk (after etching) than those predicted from the precursor solution. In Sn–Ge binary perovskite films, it has been observed that most Ge atoms accumulate at the surface since they possess smaller ionic radii than Sn atoms.[25] Likewise, Sn atoms with smaller ionic radii than Pb atoms tend to accumulate at the top surface of the FA-based Pb–Sn binary perovskite film. The Sn accumulation observed at the top surface can be ascribed to the differing crystallization dynamics of Pb- and Sn-based perovskites. Owing to the high reactivity of Sn^{2+}, the Sn-based perovskite phase crystallizes at an earlier stage during top-to-bottom film growth, resulting in a Sn-rich surface layer.[26,27]

The crystallographic phase and structure of $FAPb_{1-x}Sn_x(I_{0.8}Br_{0.2})_3$ films were analyzed by X-ray diffraction (XRD), as presented in Fig. 1c. The neat Pb sample (x = 0) was

prepared at 150 °C and yielded a reddish film. A diffraction peak at ~11.6° indicates the formation of the non-photoactive hexagonal δ-$FAPbI_3$ phase (marked with a diamond symbol), consistent with observations reposted for other mixed I–Br perovskites.[19,28] In contrast, Sn-containing wet films ($x \geq 0.2$) immediately turned black upon annealing at 100 °C. Their XRD patterns exhibit characteristic peaks that match the reported orthorhombic perovskite structure of $FASnI_3$.[29,30] The suppression of the δ-$FAPbI_3$ phase in the mixed compositions can be ascribed to the modulation of the tolerance factor (t) by Sn substitution.[31] Since the t value of $FASnI_3$ is expected to be smaller than that of δ-$FAPbI_3$, alloying pure-Pb and pure-Sn perovskites tunes t into an optimal range ($0.8 < t < 1$) and stabilizes a perovskite phase isostructural with $FASnI_3$.[32] For x = 0.2, the δ-$FAPbI_3$ peak vanishes, whereas an intense peak appears at 12.7° (marked with an asterisk symbol), attributed to residual cubic PbI_2. At higher Sn contents ($x \geq 0.4$), the XRD patterns display a single crystalline perovskite phase. Therefore, Sn incorporation facilitates the formation of the photoactive perovskite phase at a relatively low temperature. Notably, the x = 0.6 sample shows the strongest diffraction peak, signifying the highest crystallinity.

The surface morphology of the prepared perovskite film was investigated by scanning electron microscopy (SEM). As shown in Fig. 2a (high magnification) and Fig. S2 (low magnification), the neat Sn film (x = 1.0) contained large grains but also plenty of voids. The other compositions (x = 0–0.8) all exhibited complete surface coverage and densely packed grains. Additionally, Pb-containing films demonstrated smaller grains than the pure Sn film. The morphology of the pure Sn perovskite film is attributed to its rapid crystallization rate.[33,34] The incorporation of Pb might slow down the Sn-induced crystallization, thus improving the morphology of Pb–Sn binary perovskite films.

The bandgap values (E_g) of $FAPb_{1-x}Sn_x(I_{0.8}Br_{0.2})_3$ perovskites were determined by fitting their Tauc plots (Fig. S3a). Alternatively, E_g can be estimated from EQE spectra (Fig. S3b). As seen in Fig. 2b, E_g obtained from EQE spectra well agree with E_g extracted from Tauc plots, with a negligible variance of less than 0.05 eV. The abnormally high E_g of the neat Pb sample is associated with the δ-$FAPbI_3$ phase, as confirmed by its XRD pattern. Reportedly, δ-$FAPbI_3$ possesses a wide bandgap exceeding 2 eV.[18] In terms of mixed Pb–Sn samples, their E_g are in the range of 1.39–1.44 eV. Especially for the x = 0.4 and 0.6 samples, their bandgaps (~1.4 eV) fall within the ideal range of 1.3–1.4 eV, aligning with the Shockley–Queisser limit for optimal energy harvesting.[12] Moreover, it is manifested that the bandgap varies non-linearly as the x value is progressively tuned from 0.2 to 1.0. Such bandgap evolution is consistent with previous observations in most mixed Pb–Sn triiodide perovskite systems.[8–10] According to Prof. Kanatzidis's findings based on first-principles calculations, it

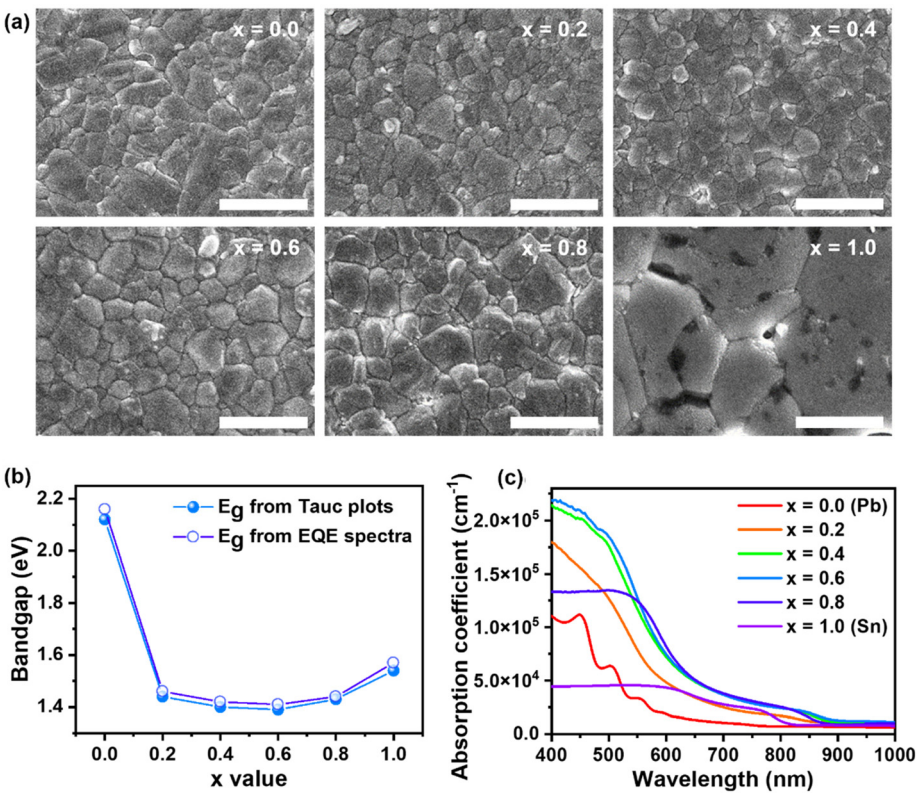

Fig. 2 Film characterization. (a) Top-view SEM images of $FAPb_{1-x}Sn_x(I_{0.8}Br_{0.2})_3$ perovskite films, where the scale bar represents 1 μm. (b) Bandgaps extracted from Tauc plots and EQE spectra, and (c) absorption coefficient spectra for $FAPb_{1-x}Sn_x(I_{0.8}Br_{0.2})_3$ perovskites.

can be attributed to a competition between the bandgap reduction caused by the spin–orbit coupling of Pb^{2+} and Sn^{2+} ions and the bandgap increase induced by lattice distortions.[35]

Absorption coefficients were calculated according to the Beer–Lambert law (see Experimental section for details). In Fig. 2c, the absorption coefficient spectrum of the neat Pb sample exhibits multiple absorption crests but no characteristic perovskite absorption onset, further confirming its non-photoactive δ-$FAPbI_3$ phase. It is noticeable that mixed Pb–Sn perovskites (x = 0.4–0.8) demonstrate higher absorption coefficients than the neat Sn perovskite across the entire spectra range of 500–900 nm. This absorption coefficient enhancement can be related to the electronic structure altering derived from the composition engineering through Pb–Sn alloy.[23,36]

The ambient stability of the studied perovskite films was demonstrated in Fig. S4, which was evaluated *via* time-resolved UV-Vis absorption measurements.[25] It shows the fraction of absorbance remained (A/A_0) at 500 nm as a function of time. After one-hour exposure to ambient air, 100%, 100%, 99%, 95%, 92% and 87% of A/A_0 was given by the film sample with x = 0, 0.2, 0.4, 0.6, 0.8 and 1.0, respectively. It is noticeable that the Pb-rich perovskite (x = 0.4) retained its absorbance for nearly one hour, whereas the Sn-rich perovskite (x = 0.6) lost 5% of its initial absorbance. Thus, improved ambient stability is found in Pb–Sn binary perovskites with reduced Sn contents owing to a lower propensity for Sn oxidation. To enhance the stability of the Pb–Sn binary perovskites, a co-additive could be added into the perovskite precursor. Additionally, a compatible passivator could be employed during post-treatment to fabricate highly efficient and stable PSCs. The completed devices could also be encapsulated with an appropriate UV-curable epoxy/glass stack for long-term outdoor operation.

Photovoltaic performance of PSCs

The photovoltaic performance of $FAPb_{1-x}Sn_x(I_{0.8}Br_{0.2})_3$ PSCs with a planar p-i-n architecture was systematically evaluated. The device architecture is illustrated in Fig. 3a, where PEDOT:PSS and $PC_{61}BM$ serve as the hole transport layer (HTL) and electron transport layer (ETL), respectively. Fig. 3b presents the energy-level diagram of the functional layers in these devices, where the valence band maximum (VBM) energy level was determined *via* photoemission spectroscopy in air (Fig. S5), while the conduction band minimum (CBM) level was estimated by adding E_g on VBM. It is found that both VBM and CBM gradually shift upward with increasing Sn content ($x \geq 0.2$). For $x \geq 0.8$, the VBM of perovskite is slightly higher than the highest occupied molecular orbital (HOMO) level of PEDOT:PSS. According to previous theoretical analysis, a band offset of less than 0.2 eV between HTL and perovskite can still help to yield efficient PSCs by reducing interfacial recombination.[37] Therefore, PEDOT:PSS and $PC_{61}BM$ are suitable for extracting holes and electrons in all Sn-incorporated PSCs ($x \geq 0.2$), respectively.

The J–V curves of the highest-performing devices with various Sn contents (x = 0–1.0) are shown in Fig. 3c, and the corresponding device parameters are listed in Table S1. The variation in the photovoltaic parameters with Sn content is further illustrated in Fig. S6, which demonstrates that the reproducibility of device performance is independent of the Sn/Pb ratio. The short-circuit current density (J_{sc}) derived from

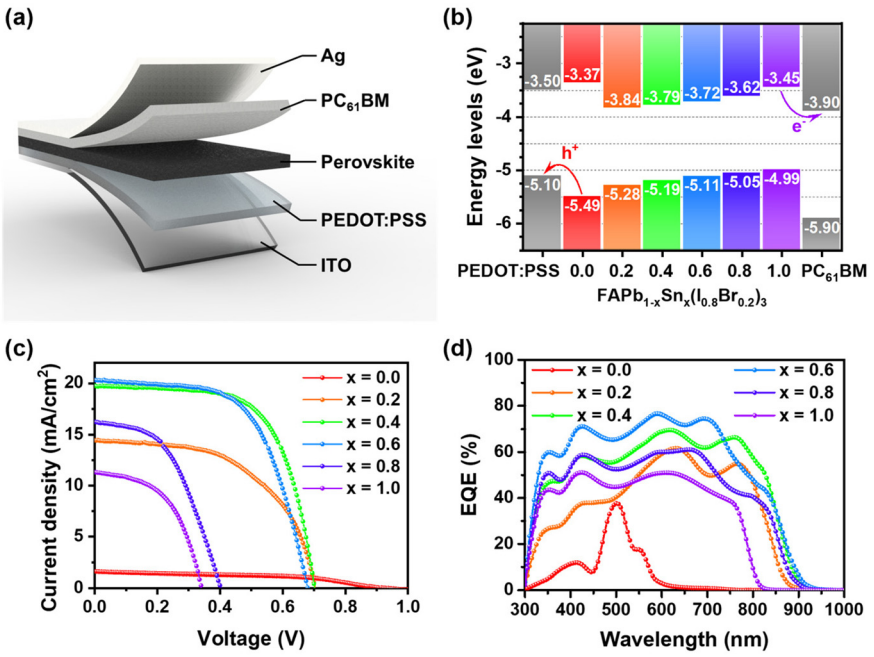

Fig. 3 Device performance. (a) Schematic diagram of the device architecture. (b) Band alignment between $FAPb_{1-x}Sn_x(I_{0.8}Br_{0.2})_3$ perovskites and the applied charge transport materials. The band values of PEDOT:PSS and $PC_{61}BM$ come from literature.[2] (c) J–V characteristics and (d) EQE spectra for $FAPb_{1-x}Sn_x(I_{0.8}Br_{0.2})_3$-based PSCs.

J–V measurements was validated by integrating the EQE spectra, with both methods yielding consistent trends in J_{sc} as a function of Sn content. The EQE spectra in Fig. 3d exhibit a distinct concave–convex profile, which has been observed in previous reports and can be ascribed to optical interference effects in planar solar cells.[38] Previous cavity-modelling studies have revealed that the EQE shape and the J_{sc} value depend strongly on device geometry, particularly on the perovskite layer thickness.[23,38] Moreover, the EQE spectra provide the information on the energy width of the absorption edge, referred to as Urbach energy (E_U).[39] Fig. S7 shows that all Sn-containing perovskites manifest significantly lower E_U values than the neat Pb perovskite (81.7 meV). According to the above XRD result, the neat Pb perovskite failed to form a photoactive perovskite phase, resulting in its high E_U and poor PCE. Along with the increasing Sn content from 0.2 to 1.0, E_U gradually falls from 25.6 meV to 20.2 meV, implying that the electronic disorder reduces and the semiconductor quality improves with the increasing Sn incorporation.[39,40]

Among the devices examined, the x = 0.4 and 0.6 PSCs surpassed the other devices, regarding PCE, J_{sc}, open-circuit voltage (V_{oc}) and fill factor (FF), with their bandgaps closer to 1.4 eV. The enhanced performance of these devices (x = 0.4 and 0.6) can be attributed to their near-optimal bandgaps, proper band alignment and superior crystallinity, together with void-free, dense film morphology. It is noteworthy that the x = 0.4 device achieved the highest PCE of nearly 9%, coupled with the lowest photovoltage loss (V_{oc} loss = $E_g - qV_{oc}$) of 0.70 V. In comparison, the x = 0.6 device exhibited a slightly lower PCE and a comparable V_{oc} loss of 0.71 V. While it generated the highest J_{sc} of 20.39 mA cm^{-2}, likely due to its higher absorption coefficients (Fig. 2c).

Furthermore, the cross-sectional SEM image of PSCs based on the optimal composition, $FAPb_{0.6}Sn_{0.4}(I_{0.8}Br_{0.2})_3$, (Fig. S8a) showed a thin, pinhole-free perovskite layer with a thickness of only 360 nm. Previous studies have demonstrated that thicker perovskite films exhibit enhanced light absorption, leading to increased photocurrent generation.[11,23] To further improve the photovoltaic performance, we adopted a perovskite thickening strategy. By incorporating a 500 nm-thick perovskite layer (Fig. S8b), the J_{sc} of the x = 0.4 device increased to 22.13 mA cm^{-2}. Remarkably, this device yielded a champion PCE of 10.27% under reverse scan and 10.07% under forward scan (Fig. S9) in ambient air, suggesting a negligible hysteresis.

Charge recombination mechanism

To further understand the significant V_{oc} deficit of the $FAPb_{1-x}Sn_x(I_{0.8}Br_{0.2})_3$ PSCs (x = 0.4 and 0.6) with near-optimal bandgaps (~1.4 eV), their recombination mechanism were investigated *via* multiple electrical characterizations. The ideality factor (n) determined by Suns-V_{oc} method was used to elucidate the recombination mechanism that governs the photovoltaic performance of PSCs. Fig. 4a presents the plots of V_{oc} as a function of light intensity (L) on a semi-logarithmic scale, where n values were calculated from the slope of the fitting line according to the expression of $\Delta V_{oc}/\Delta \ln L) = n \cdot k_B T/q$ (q is electron charge, k_B is Boltzmann constant, and T is temperature).[41,42] In the extreme cases, n = 1 represents bimo-

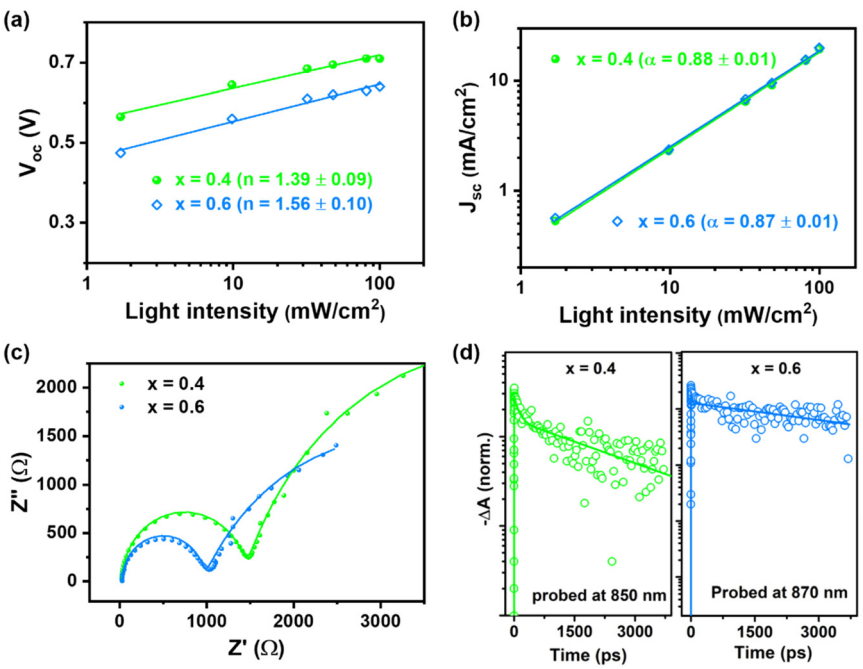

Fig. 4 Charge recombination. The light intensity dependence of (a) V_{oc} and (b) J_{sc} for PSCs based on $FAPb_{1-x}Sn_x(I_{0.8}Br_{0.2})_3$ (x = 0.4 and 0.6). (c) Nyquist plots of $FAPb_{1-x}Sn_x(I_{0.8}Br_{0.2})_3$ PSCs with x = 0.4 and 0.6, measured under 0.9 sun illumination without bias. The solid spheres represent the data obtained and solid lines represent the fitting curves. (d) TA dynamics of $FAPb_{1-x}Sn_x(I_{0.8}Br_{0.2})_3$ perovskite films, where x = 0.4 and 0.6. Solid lines are bi-exponential fittings.

lecular (or radiative) recombination, whereas n = 2 signifies Shockley–Read–Hall (SRH) recombination. Trap-assisted SRH recombination has been frequently revealed as the dominant recombination in most PSCs.[23,39] For $FAPb_{1-x}Sn_x(I_{0.8}Br_{0.2})_3$ PSCs, the x = 0.4 and 0.6 devices yielded n values of 1.39 and 1.59, respectively. The higher n value for x = 0.6 indicates that trap-assisted recombination is more pronounced in the $FAPb_{0.4}Sn_{0.6}(I_{0.8}Br_{0.2})_3$ device, contributing to its slightly larger V_{oc} loss.

Following the identification of dominant recombination type at open circuit, the recombination process at short circuit was further investigated based on the relationship between J_{sc} and L. In Fig. 4b, the J_{sc} against L in log scale was fitted to a power law dependence of $J_{sc} \propto L^{\alpha}$. Compared with the x = 0.6 device, the x = 0.4 device shows a slightly higher α value, signifying more efficient charge collection under the short-circuit condition and hence a lower V_{oc} loss. Moreover, deviations of α from unity can be ascribed to energy barriers, space charge defects, and mobility differences between electrons and holes.[43]

In addition, the recombination dynamics was analyzed by measuring the EIS of the highly performing mixed Pb–Sn PSCs. The obtained Nyquist plots are illustrated in Fig. 4c, and the electrical equivalent circuits employed for fitting are portrayed in Fig. S10. Notably, a constant phase element (CPE) rather than an ideal capacitor was employed in the low frequency range for more accurate fitting. The fitting results are summarized in Table S2, where the recombination resistance (R_{rec}) equals to the summation of R_{HF} and R_{LF}. R_{rec} describes recombination process at the interface and within the perovskite layer, whereas R_{HVF} and R_{LF} correspond to high-frequency and low-frequency resistance capacitance, respectively.[44–46] Comparing the R_{rec} values of the examined devices, the device with x = 0.4 exhibits higher R_{rec}. It suggests a reduced recombination in the x = 0.4 solar cell, which is consistent with its low V_{oc} loss.

Apart from the recombination dynamics in the whole device, the photoexcited-charge-carrier dynamics within the perovskite layer was further investigated *via* transient absorption (TA) spectroscopy.[47] The TA dynamics in Fig. 4d were well fitted using two exponential time constants (τ_1 and τ_2) and respective amplitudes (A_1 and A_2). The average carrier lifetime (τ_{ave}) was determined by the expression of $\tau_{ave} = A_1\tau_1 + A_2\tau_2$, and the calculated results were listed in Table S3. It reveals that the slow decay lifetime (τ_2) dominates the overall decay lifetime as $A_2 > A_1$. Additionally, τ_{ave} rises from 1.5 ± 0.2 ns to 2.7 ± 0.3 ns as the Sn content increases from 0.4 to 0.6, suggesting prolonged carrier lifetime and reduced recombination rate in the x = 0.6 perovskite film.

Overall, light-intensity-dependent J–V and EIS results indicate that the Pb-rich device (x = 0.4) experiences more efficient charge collection and less severe trap-assisted recombination than the Sn-rich device (x = 0.6). This leads to lower energy losses in the Pb-rich device, which is consistent with its lower V_{oc} loss. As discussed before, the Pb-rich perovskite demonstrates lower VBM than the Sn-rich perovskite and larger band offset with respect to PEDOT:PSS, facilitating the charge transport at the HTL/perovskite interface.[48] Interestingly, the τ_{ave} value for the Pb-rich perovskite film (x = 0.4) suggests faster bulk recombination than that of the Sn-rich perovskite film (x = 0.6). Consistently, the E_U estimation implies a higher density of Urbach tail states in the Pb-rich perovskite. It is well established that structural and compositional disorder in perovskite films introduces Urbach tail states that can act as non-radiative recombination centers.[49,50] Crystallographic analysis reveals that the Pb-rich perovskite exhibits poorer crystallinity, as evidenced by lower peak intensities and a broader full width at half maximum (FWHM) (Fig. S11). Additionally, the Williamson–Hall plot yields a larger relative strain (ε) for the Pb-rich perovskite (Fig. S12), corroborating its greater structural disorder. We therefore attribute the V_{oc} deficit to two counteracting factors: (i) structural disorder and (ii) band alignment between the perovskite and the charge selective contacts. Compared with the x = 0.6 composition, the perovskite with optimal Sn content (x = 0.4) possesses a higher degree of structural and electronic disorder, which accelerates bulk recombination inside the perovskite layer. Meanwhile, the x = 0.4 composition establishes a favourable band alignment with the HTL, suppressing interfacial recombination and thereby enhancing the overall charge collection efficiency of the complete device. Owing to the counterbalance between these opposing effects, devices with x = 0.4 and 0.6 exhibit comparable V_{oc} deficits.

Conclusions

In summary, we have developed a series of pure FA-based Pb–Sn binary perovskites, namely $FAPb_{1-x}Sn_x(I_{0.8}Br_{0.2})_3$ (x = 0.2, 0.4, 0.6 and 0.8), with near-optimal bandgaps (1.39–1.44 eV) through compositional engineering. Remarkably, the perovskite film with x = 0.4 possesses uniform, pinhole-free morphology, enhanced absorption coefficients, and proper band alignment with typical charge transport materials. It also demonstrates superior air stability compared with the Sn-rich perovskite films ($x \geq 0.6$). Consequently, PSCs employing this optimal Sn content (x = 0.4) achieve the highest PCE among all devices tested under ambient air. Moreover, on the basis of evaluating the recombination in both perovskite film and full device, we found that the V_{oc} deficit is influenced by two competing factors. For x = 0.4 perovskites, higher structural disorder accelerates charge recombination within the perovskite layer, while their proper band alignment effectively suppresses interfacial recombination. Therefore, their device performance could be further improved by reducing structural disorder through strategies such as enhancing perovskite crystallinity and bulk defect passivation. Overall, this work advances the understanding of Sn incorporation in Pb–Sn binary perovskites, particularly in relation to recombination mechanisms. By demonstrating the viability of Pb–Sn binary perovskites with near-optimal bandgaps, our results shed light on the development of environmentally benign single-junction and tandem solar cells, in line with broader efforts to reduce reliance on toxic Pb-based perovskites.

Author contributions

Yan Chen: conceptualization, investigation, visualization, and writing – original draft. Ying Fan Tay: investigation and visualization. Mingjie Li: investigation and visualization. Than Saw Oo: writing – review & editing. Sing Yang Chiam: investigation. Yeng Ming Lam: resources. Tze Chien Sum: supervision and writing – review & editing. Lydia Helena Wong: supervision, resources, and writing – review & editing.

Conflicts of interest

There are no conflicts of interest to declare.

Data availability

The data supporting this work are included in the main article and its supplementary information (SI). Supplementary information is available. See DOI: https://doi.org/10.1039/d5nr02776d.

Acknowledgements

This work was supported by the Singapore-Berkeley Research Initiative for Sustainable Energy (SinBeRISE) CREATE Program. Also it was funded by Shandong Postdoctoral Science Foundation (SDBX202302001) and Shandong Provincial Nature Science Foundation (ZR2023QE306). The authors acknowledge the Facility for Analysis Characterization Testing & Simulation (FACTS) for their assistance with characterization techniques. Furthermore, the authors are grateful for the insightful discussions with Prof. Nripan Mathews, Prof. Subodh Gautam Mhaisalkar and Dr Shreyash Sudhakar Hadke.

References

1 J. Han, K. Park, S. Tan, Y. Vaynzof, J. Xue, E. W.-G. Diau, M. G. Bawendi, J.-W. Lee and I. Jeon, *Nat. Rev. Methods Primers*, 2025, **5**, 3.
2 Q. Jiang and K. Zhu, *Nat. Rev. Mater.*, 2024, **9**, 399–419.
3 I. López-Fernández, D. Valli, C.-Y. Wang, S. Samanta, T. Okamoto, Y.-T. Huang, K. Sun, Y. Liu, V. S. Chirvony, A. Patra, J. Zito, L. De Trizio, D. Gaur, H.-T. Sun, Z. Xia, X. Li, H. Zeng, I. Mora-Seró, N. Pradhan, J. P. Martínez-Pastor, P. Müller-Buschbaum, V. Biju, T. Debnath, M. Saliba, E. Debroye, R. L. Z. Hoye, I. Infante, L. Manna and L. Polavarapu, *Adv. Funct. Mater.*, 2024, **34**, 2307896.
4 X. Jiang, F. Wang, Q. Wei, H. Li, Y. Shang, W. Zhou, C. Wang, P. Cheng, Q. Chen, L. Chen and Z. Ning, *Nat. Commun.*, 2020, **11**, 1245.
5 J. Chen, J. Luo, E. Hou, P. Song, Y. Li, C. Sun, W. Feng, S. Cheng, H. Zhang, L. Xie, C. Tian and Z. Wei, *Nat. Photonics*, 2024, **18**, 464–470.
6 T. Krishnamoorthy, H. Ding, C. Yan, L. L. Wei, T. Baikie, Z. Zhang, M. Sherburne, S. Li, M. Asta and N. Mathews, *J. Mater. Chem. A*, 2015, **3**, 23829–23832.
7 I. Kopacic, B. Friesenbichler, S. F. Hoefler, B. Kunert, H. Plank, T. Rath and G. Trimmel, *ACS Appl. Energy Mater.*, 2018, **1**, 343–347.
8 X. Jia, D. Yang, D. Zheng, Z. Chang, J. Liu, L. Liu, L. Peng, Y. Tong, K. Wang and S. Liu, *Chem*, 2025, **11**, 102384.
9 F. Hao, C. C. Stoumpos, R. P. Chang and M. G. Kanatzidis, *J. Am. Chem. Soc.*, 2014, **136**, 8094–8099.
10 G. E. Eperon, T. Leijtens, K. A. Bush, R. Prasanna, T. Green, J. T.-W. Wang, D. P. McMeekin, G. Volonakis, R. L. Milot, R. May, A. Palmstrom, D. J. Slotcavage, R. A. Belisle, J. B. Patel, E. S. Parrott, R. J. Sutton, W. Ma, F. Moghadam, B. Conings, A. Babayigit, H.-G. Boyen, S. Bent, F. Giustino, L. M. Herz, M. B. Johnston, M. D. McGehee and H. J. Snaith, *Science*, 2016, **354**, 861.
11 D. Zhao, Y. Yu, C. Wang, W. Liao, N. Shrestha, C. R. Grice, A. J. Cimaroli, L. Guan, R. J. Ellingson, K. Zhu, X. Zhao, R.-G. Xiong and Y. Yan, *Nat. Energy*, 2017, **2**, 17018.
12 I. M. Peters and T. Buonassisi, *Joule*, 2018, **2**, 1160–1170.
13 S. Yoon, J. Ryu, S. Cho, H. D. Kim, J. Lim, J. S. Cho, J. Park and D.-W. Kang, *Small*, 2025, 2501876, DOI: 10.1002/smll.202501876.
14 Q. Sun, Z. Zhang, T. Zhang, Y. Feng, A. Gu, H. Yu, M. Zhang, X. L. Zhang, J. Zhu, Y. Shen and M. Wang, *ACS Energy Lett.*, 2022, **7**, 4215–4223.
15 Y. Zhang, Y. Chen, G. Liu, Y. Wu, Z. Guo, R. Fan, K. Li, H. Liu, Y. Zhao, T. Kodalle, Y. Chen, C. Zhu, Y. Bai, Q. Chen and H. Zhou, *Science*, 2025, **387**, 284–290.
16 C. Wang, F. Gu, Z. Zhao, H. Rao, Y. Qiu, Z. Cai, G. Zhan, X. Li, B. Sun, X. Yu, B. Zhao, Z. Liu, Z. Bian and C. Huang, *Adv. Mater.*, 2020, **32**, 1907623.
17 D. Chi, S. Huang, M. Zhang, S. Mu, Y. Zhao, Y. Chen and J. You, *Adv. Funct. Mater.*, 2018, **28**, 1804603.
18 N. J. Jeon, J. H. Noh, W. S. Yang, Y. C. Kim, S. Ryu, J. Seo and S. I. Seok, *Nature*, 2015, **517**, 476.
19 M. Saliba, T. Matsui, J. Y. Seo, K. Domanski, J. P. Correa-Baena, M. K. Nazeeruddin, S. M. Zakeeruddin, W. Tress, A. Abate, A. Hagfeldt and M. Gratzel, *Energy Environ. Sci.*, 2016, **9**, 1989–1997.
20 S. Lee and D.-W. Kang, *ACS Appl. Mater. Interfaces*, 2017, **9**, 22432–22439.
21 S. Lee, J. Moon, J. Ryu, B. Parida, S. Yoon, D.-G. Lee, J. S. Cho, S. Hayase and D.-W. Kang, *Nano Energy*, 2020, **77**, 105309.
22 Y. Shang, X. Li, W. Lian, X. Jiang, X. Wang, T. Chen, Z. Xiao, M. Wang, Y. Lu and S. Yang, *Chem. Eng. J.*, 2023, **457**, 141246.
23 Z. Yang, A. Rajagopal and A. K. Jen, *Adv. Mater.*, 2017, **29**, 1704418.
24 S. Gupta, D. Cahen and G. Hodes, *J. Phys. Chem. C*, 2018, **122**, 13926–13936.
25 N. Ito, M. A. Kamarudin, D. Hirotani, Y. Zhang, Q. Shen, Y. Ogomi, S. Iikubo, T. Minemoto, K. Yoshino and S. Hayase, *J. Phys. Chem. Lett.*, 2018, **9**, 1682–1688.

26 S. Chen, X. Xiao, B. Chen, L. L. Kelly, J. Zhao, Y. Lin, M. F. Toney and J. Huang, *Sci. Adv.*, 2021, **7**, eabb2412.
27 K. Liang, D. B. Mitzi and M. T. Prikas, *Chem. Mater.*, 1998, **10**, 403–411.
28 D. P. McMeekin, G. Sadoughi, W. Rehman, G. E. Eperon, M. Saliba, M. T. Hörantner, A. Haghighirad, N. Sakai, L. Korte, B. Rech, M. B. Johnston, L. M. Herz and H. J. Snaith, *Science*, 2016, **351**, 151–155.
29 W. Liao, D. Zhao, Y. Yu, C. R. Grice, C. Wang, A. J. Cimaroli, P. Schulz, W. Meng, K. Zhu, R. G. Xiong and Y. Yan, *Adv. Mater.*, 2016, **28**, 9333–9340.
30 S. J. Lee, S. S. Shin, Y. C. Kim, D. Kim, T. K. Ahn, J. H. Noh, J. Seo and S. I. Seok, *J. Am. Chem. Soc.*, 2016, **138**, 3974–3977.
31 J. Liu, G. Wang, Z. Song, X. He, K. Luo, Q. Ye, C. Liao and J. Mei, *J. Mater. Chem. A*, 2017, **5**, 9097–9106.
32 Z. Li, M. Yang, J.-S. Park, S.-H. Wei, J. J. Berry and K. Zhu, *Chem. Mater.*, 2016, **28**, 284–292.
33 N. K. Noel, S. D. Stranks, A. Abate, C. Wehrenfennig, S. Guarnera, A.-A. Haghighirad, A. Sadhanala, G. E. Eperon, S. K. Pathak, M. B. Johnston, A. Petrozza, L. M. Herz and H. J. Snaith, *Energy Environ. Sci.*, 2014, **7**, 3061–3068.
34 F. Hao, C. C. Stoumpos, P. Guo, N. Zhou, T. J. Marks, R. P. H. Chang and M. G. Kanatzidis, *J. Am. Chem. Soc.*, 2015, **137**, 11445–11452.
35 J. Im, C. C. Stoumpos, H. Jin, A. J. Freeman and M. G. Kanatzidis, *J. Phys. Chem. Lett.*, 2015, **6**, 3503–3509.
36 W.-J. Yin, J.-H. Yang, J. Kang, Y. Yan and S.-H. Wei, *J. Mater. Chem. A*, 2015, **3**, 8926–8942.
37 T. Minemoto and M. Murata, *Sol. Energy Mater. Sol. Cells*, 2015, **133**, 8–14.
38 Q. Lin, A. Armin, R. C. R. Nagiri, P. L. Burn and P. Meredith, *Nat. Photonics*, 2015, **9**, 106–112.
39 B. Zhao, M. Abdi-Jalebi, M. Tabachnyk, H. Glass, V. S. Kamboj, W. Nie, A. J. Pearson, Y. Puttisong, K. C. Gödel, H. E. Beere, D. A. Ritchie, A. D. Mohite, S. E. Dutton, R. H. Friend and A. Sadhanala, *Adv. Mater.*, 2016, **29**, 1604744.
40 J. T.-W. Wang, Z. Wang, S. Pathak, W. Zhang, D. W. deQuilettes, F. Wisnivesky-Rocca-Rivarola, J. Huang, P. K. Nayak, J. B. Patel, H. A. Mohd Yusof, Y. Vaynzof, R. Zhu, I. Ramirez, J. Zhang, C. Ducati, C. Grovenor, M. B. Johnston, D. S. Ginger, R. J. Nicholas and H. J. Snaith, *Energy Environ. Sci.*, 2016, **9**, 2892–2901.
41 H. J. Snaith, L. Schmidt-Mende, M. Grätzel and M. Chiesa, *Phys. Rev. B: Condens. Matter Mater. Phys.*, 2006, **74**, 045306.
42 S. R. Cowan, A. Roy and A. J. Heeger, *Phys. Rev. B: Condens. Matter Mater. Phys.*, 2010, **82**, 245207.
43 A. K. K. Kyaw, D. H. Wang, V. Gupta, W. L. Leong, L. Ke, G. C. Bazan and A. J. Heeger, *ACS Nano*, 2013, **7**, 4569–4577.
44 I. Zarazua, G. Han, P. P. Boix, S. Mhaisalkar, F. Fabregat-Santiago, I. Mora-Sero, J. Bisquert and G. Garcia-Belmonte, *J. Phys. Chem. Lett.*, 2016, **7**, 5105–5113.
45 D. Prochowicz, M. M. Tavakoli, A. Solanki, T. W. Goh, K. Pandey, T. C. Sum, M. Saliba and P. Yadav, *J. Mater. Chem. A*, 2018, **6**, 14307–14314.
46 L. Contreras-Bernal, S. Ramos-Terrón, A. Riquelme, P. P. Boix, J. Idígoras, I. Mora-Seró and J. A. Anta, *J. Mater. Chem. A*, 2019, **7**, 12191–12200.
47 G. Xing, N. Mathews, S. Sun, S. S. Lim, Y. M. Lam, M. Grätzel, S. Mhaisalkar and T. C. Sum, *Science*, 2013, **342**, 344.
48 M. Stolterfoht, P. Caprioglio, C. M. Wolff, J. A. Márquez, J. Nordmann, S. Zhang, D. Rothhardt, U. Hörmann, Y. Amir, A. Redinger, L. Kegelmann, F. Zu, S. Albrecht, N. Koch, T. Kirchartz, M. Saliba, T. Unold and D. Neher, *Energy Environ. Sci.*, 2019, **12**, 2778–2788.
49 S. De Wolf, J. Holovsky, S.-J. Moon, P. Löper, B. Niesen, M. Ledinsky, F.-J. Haug, J.-H. Yum and C. Ballif, *J. Phys. Chem. Lett.*, 2014, **5**, 1035–1039.
50 J. Park, B. J. Kang, G. Seo, J. Kim, T. G. Park, S. Nam, J. J. Yoo, K. Lee, Y. U. Jeong, M. Park, S. S. Shin and F. Rotermund, *Adv. Energy Mater.*, 2025, **15**, 2400225.